

Electronic supplementary information for:

Exceeding Milli-Watt Powering Magneto-Mechano-Electric Generator for Standalone-Powered Electronics

Venkateswarlu Annapureddy^{a†}, Suok-Min Na^{b†}, Geon-Tae Hwang^a, Min Gyu Kang^c, Rammohan Sriramdas^c, Haribabu Palneedi^a, Woon-Ha Yoon^a, Byung-Dong Hahn^a, Jong-Woo Kim^a, Cheol-Woo Ahn^a, Dong-Soo Park^a, Jong-Jin Choi^a, Dae-Yong Jeong^d, Alison B. Flatau^b, Mahesh Peddigari^a, Shashank Priya^{e*}, Kwang-Ho Kim^{f*}, and Jungho Ryu^{g*}

^a. Functional Ceramics Group, Korea Institute of Materials Science (KIMS), Changwon, Gyeongnam 51508, Republic of Korea

^b. Department of Aerospace Engineering, University of Maryland, College Park, MD 20742, USA

^c. Bio-inspired Materials and Devices Laboratory (BMDL), Center for Energy Harvesting Materials and Systems (CEHMS), Virginia Tech, Blacksburg, Virginia 24061, USA

^d. Department of Materials Science & Engineering, Inha University, Incheon 22212, Republic of Korea.

^e. Department of Materials Science & Engineering, Pennsylvania State University, University Park, PA 16802, USA

^f. School of Materials Science and Engineering, Pusan National University, Busan 46241, Republic of Korea

^g. School of Materials Science and Engineering, Yeungnam University, Gyeongsan, Gyeongbuk 38541, Republic of Korea

[†] VA and SMN contributed equally to this work.

*Corresponding authors SP (spriya@vt.edu) KHK (kwhokim@pusan.ac.kr), JR (puggy96@hanmail.net)

This file includes:

S1: Energy conversion efficiency of the MME generator

Table S1: The nominal operating current of the various operating modes of the wireless IoT sensor module used in this work.

Table S2. Measured displacements of the MME generators at an excitation input magnetic field of 200 μT (2 Oe) with different frequencies.

Figures

Figure S1. Schematics of the textured Fe-Ga sheet fabrication and structural and magnetic characterization techniques. (a) Rolling of Fe-Ga Ingot, (b) atmospheric annealing the rolled sheet, (c) magnetostriction measurement using strain gauge, and (d) EBSD scan to characterize microstructure after fine polishing of the sheet.

Figure S2. Schematic XRD measurement, and measured XRD pattern of textured Fe-Ga sheet sample.

Figure S3. Magnetostriction (a) and magnetization (b) performance of the Ni sample as a function of applied magnetic field.

Figure S4. Experimental set-up for measuring vibrational deflection amplitude of the MME generator using LDV.

Figure S5. Open-circuit output voltage wave forms at different applied magnetic AC fields from 50 μT (0.5 Oe) to 225 μT (2.25 Oe) at an anti-resonance frequency of 100 Hz. The output performance of the MME generator linearly increased with the input magnetic AC field.

Figure S6. ME hysteresis characteristics ($\alpha_{ME} - H_{dc}$) of the ME cantilever structures in bending resonance mode (approximately 900 Hz). The maximum α_{ME} of the Fe-Ga-based ME composite was approximately 26 $\text{V cm}^{-1}\text{Oe}^{-1}$, which was approximately 53 % higher than that of the Ni-

based ME composite. (b) ME responses of the trilayered composites of Fe-Ga/PMN-PZ-PT/Fe-Ga and Ni/PMN-PZ-PT/Ni with similar aspect ratios of magnetostrictive layers as that of bilayered composites.

Figure S7. Phase-field model simulated domain structures (under zero magnetic bias), M-H hysteresis, and ME voltage coefficient α_{ME} for laminate PZT/Ni composite under zero mismatch strain $\varepsilon_{mis} = 0$ with varying demagnetization factors (N_d) in Ni layer of different thicknesses: (a) $N_d = 0.008$ ($t = 50 \mu\text{m}$), (b) $N_d = 0.014$ ($t = 100 \mu\text{m}$), and (c) $N_d = 0.026$ ($t = 200 \mu\text{m}$), and under mismatch strain $\varepsilon_{mis} = 0.003$ with the same demagnetization factor $N_d = 0.008$ in (d) flexural and (e) non-flexural composite. Domain patterns are visualized by color maps with red, green, blue (RGB) components proportional to P_x, P_y, P_z in PZT layer and M_x, M_y, M_z in Ni layer, respectively.

Figure S8. Model structure of the MME generators for COMSOL simulation.

Figure S9. The power developed by Ni-based MME generator as a function of load resistance using Maxwell's equations

Figure S10. Schematic circuit diagram for measuring the output performance of the generator. The designed rectifying circuit system included the Fe-Ga MME generator, bridge rectifier, a capacitor, and external load. The output current and voltage were measured using a Keithley 2612A source meter and a digital oscilloscope, respectively.

Figure S11. The output stability of the Fe-Ga MME generator under different output loads.

Figure S12. Schematic circuit diagram of the standalone-powered wireless IoT sensor system with triple-axis gyro (TAG), pressure, and temperature sensors, using the textured Fe-Ga MME generator.

Figure S13. Snapshot images of the standalone-powered electronic circuit system and various parts of a small quadrotor drone operated with our Fe-Ga MME generator.

Figure S14. Schematic for LED sign board containing 174 high-intensity red LEDs.

Figure S15. Impedance spectrum of the Fe-Ga MME generator

Other supplementary information for this manuscript

Video S1: Assembled standalone-powering circuit system and operation of wireless IoT sensor system with triple-axis gyro (TAG), pressure, and temperature sensors by the textured Fe-Ga MME generator

Video S2: Assembled standalone-powering circuit system and operation of Quadrotor Drone using the textured Fe-Ga MME generator.

S1: Energy conversion efficiency of the MME generator

The energy conversion efficiency of a MME generator is determined by the fraction of energy gathered by the magnetic layer which is converted to electricity, and is defined as Equation (S1):

$$\eta(\%) = \frac{\text{Generated electric energy}}{\text{Energy stored in magnetic material}} \times 100 = \frac{P_{AC}}{P_{in}} \times 100 \quad (S1)$$

The input power (P_{in}) is related to the incident magnetic noise energy spread through the volume of the generator. The magnetic energy collected by the MME generator is^[1,2]

$$P_{in} = \frac{2}{\mu} \iiint H^2 dx dy dz = \frac{1}{2} \times \frac{H^2}{\mu} \times v \times f \quad (S2)$$

where, H is the input magnetic field amplitude, v is the total volume of generator and f is the frequency. The volume AC power density of Fe-Ga MME generator reached 4.6 mW cm^{-3} and greater than 20% energy conversion efficiency was obtained.

Table S1. The nominal operating current of the various operating modes of the wireless IoT sensor module used in this work .

	Operation Mode	Part No./ Manufacturer	Nominal Operating Current
Display/ Microprocessor	Self Mode	-	2.7 μ A
	Welcome Screen	-	8.9 μ A
	Time and Date	-	9.0 μ A
Sensors	Temperature Sensor	CC430/ Texas Inst.	10 μ A
	Altitude/Pressure Sensor	BMA085/Bosch Sensor Tec.	18 μ A
	Gyro Sensor	BMA250/Bosch Sensor Tec.	166 μ A
Data Communication	Continuous SimpliciTL SYNC	CC1101/TI	0.9 mA
	Continuous SimpliciTL Gyro		3.7 mA

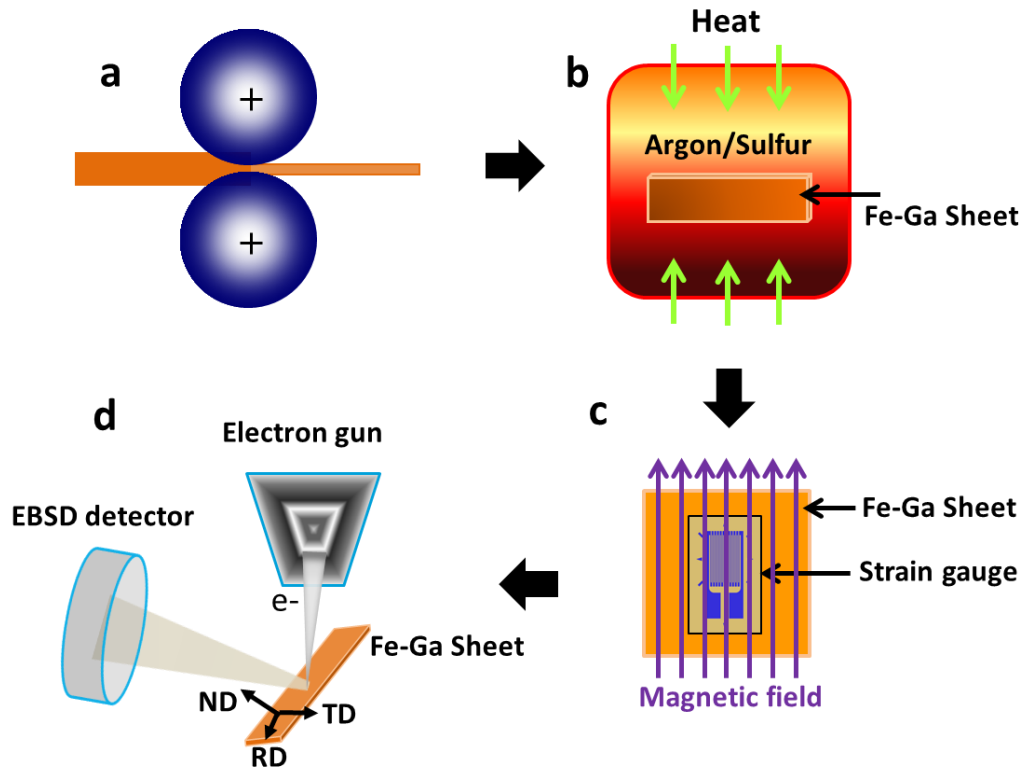


Figure S1. Schematics for the fabrication of the textured Fe-Ga sheet and structural and magnetic characterization techniques. (a) Rolling of the Fe-Ga ingot, (b) atmospheric annealing of the rolled sheet, (c) magnetostriction measurement using a strain gauge, and (d) EBSD scan to characterize the microstructure after fine polishing of the sheet.

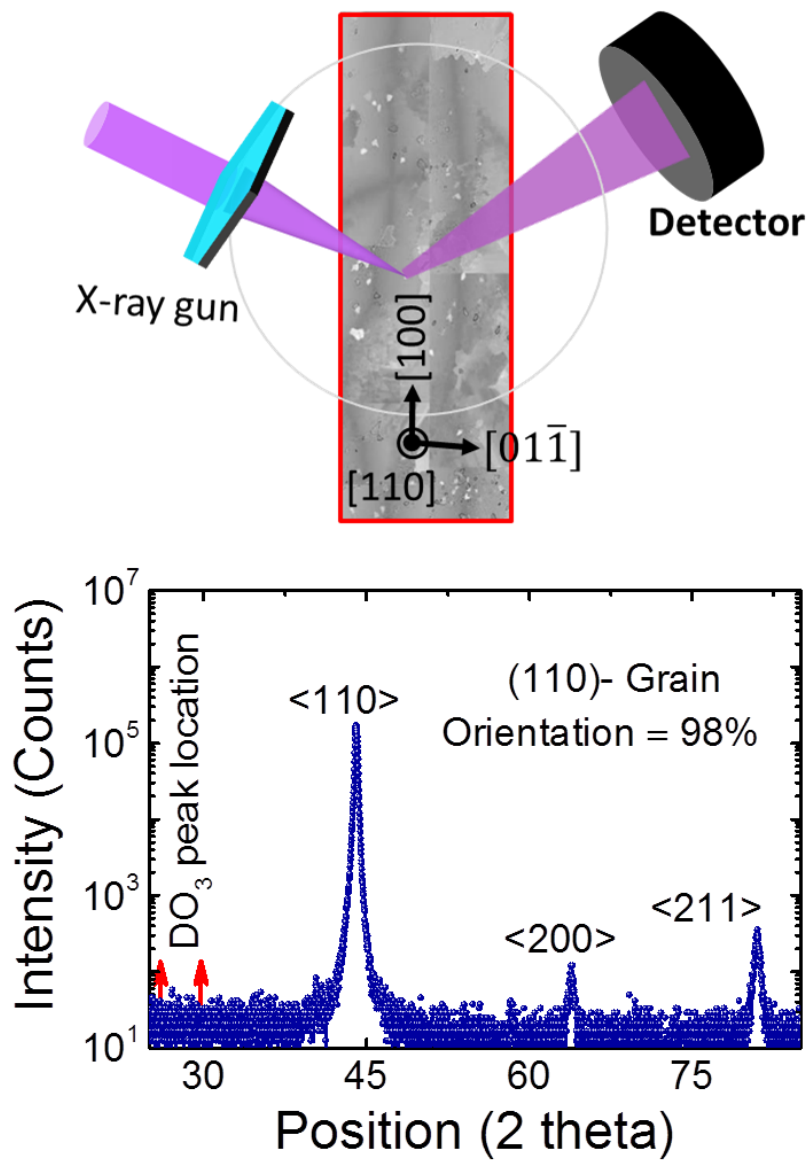


Figure S2. Schematic of the XRD measurement and measured XRD pattern of the textured Fe-Ga sheet sample.

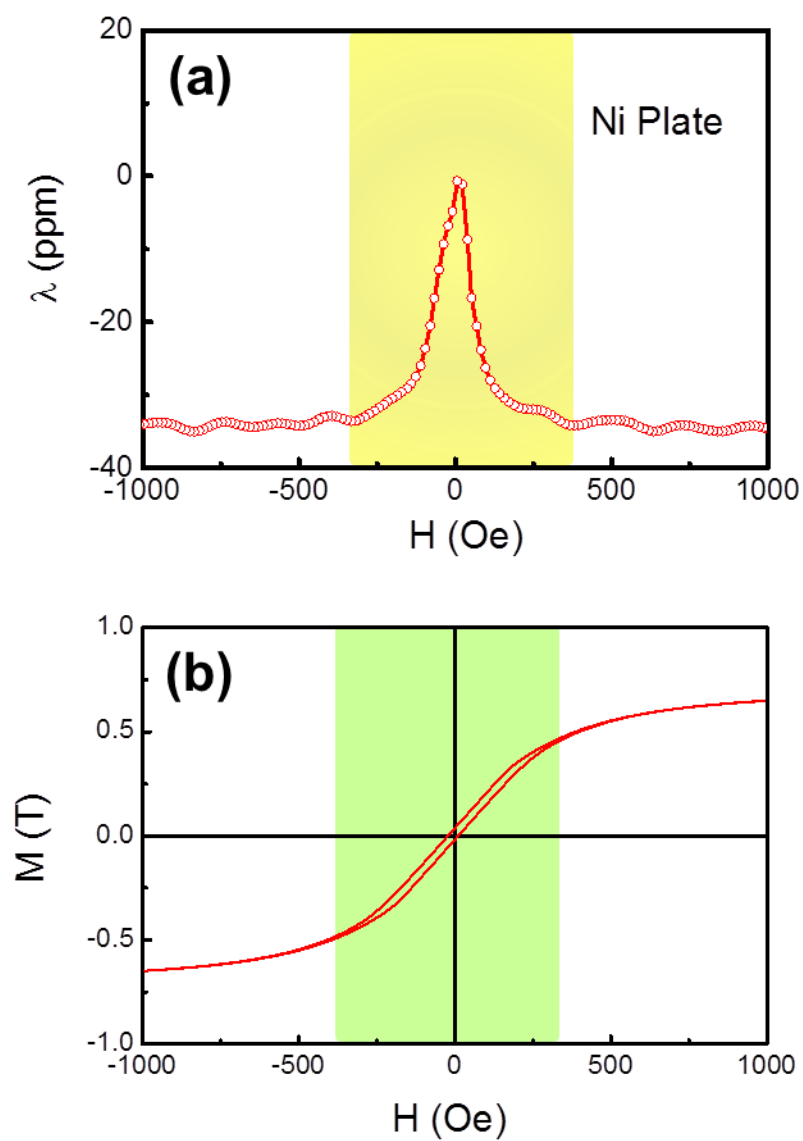


Figure S3. Magnetostriction (a) and magnetization (b) characteristics of the Ni sample as a function of applied magnetic field.

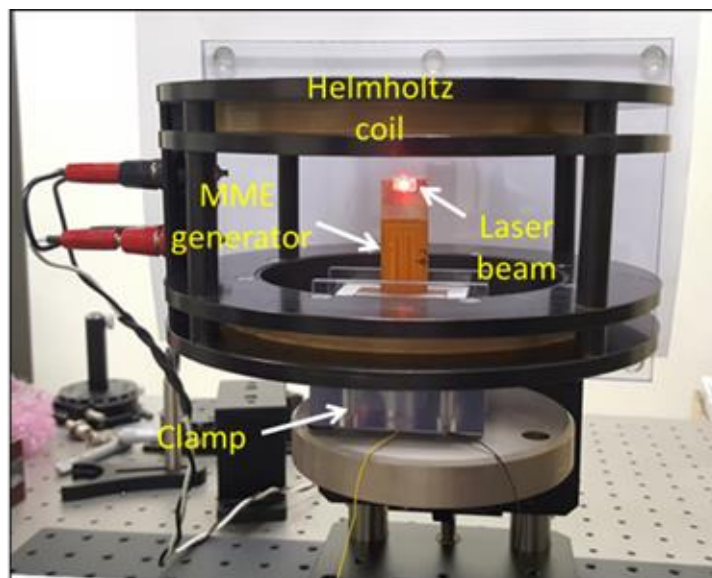


Figure S4. Experimental set-up for measuring vibrational deflection amplitude of the MME generator using LDV.

The vibrational deflection amplitudes in Z-direction of the generators were measured using a Laser Doppler Vibrometer (LDV) as shown in Figure S4. For the Fe-Ga and Ni based MME generators, maximum displacements (peak-to-peak) of 570 μm and 231 μm , respectively, were obtained at an excitation magnetic field of 200 μT with 100 Hz (Table S3). The resonance frequency of MME generator was tuned to 100 Hz, where the maximum displacement was observed. The real vibration depends on the applied magnetic field, and is less than 1 mm, in general, which is not strong enough. Therefore, it is difficult to visualize such small amplitude vibrations of the MME generator in the video files.

Table S2. Measured displacements of the MME generators at an excitation input magnetic field of 200 μT (2 Oe) with different frequencies. Since the same magnetic proof mass were used for both MME generators, the differences of deflection amplitude were mainly caused by magnetostriction behaviors of Galfenol and Nickel used in MME generators.

	Fe-Ga based MME	Ni based MME
Frequency (Hz)	Deflection Amplitude (μm)	
80	29.7	15.1
90	87.9	26.4
95	172.2	47.2
98	259	101.5
100	570	231.1
102	326.2	160.2
105	202.7	62.7
110	51.9	27.6
120	21.3	11.7

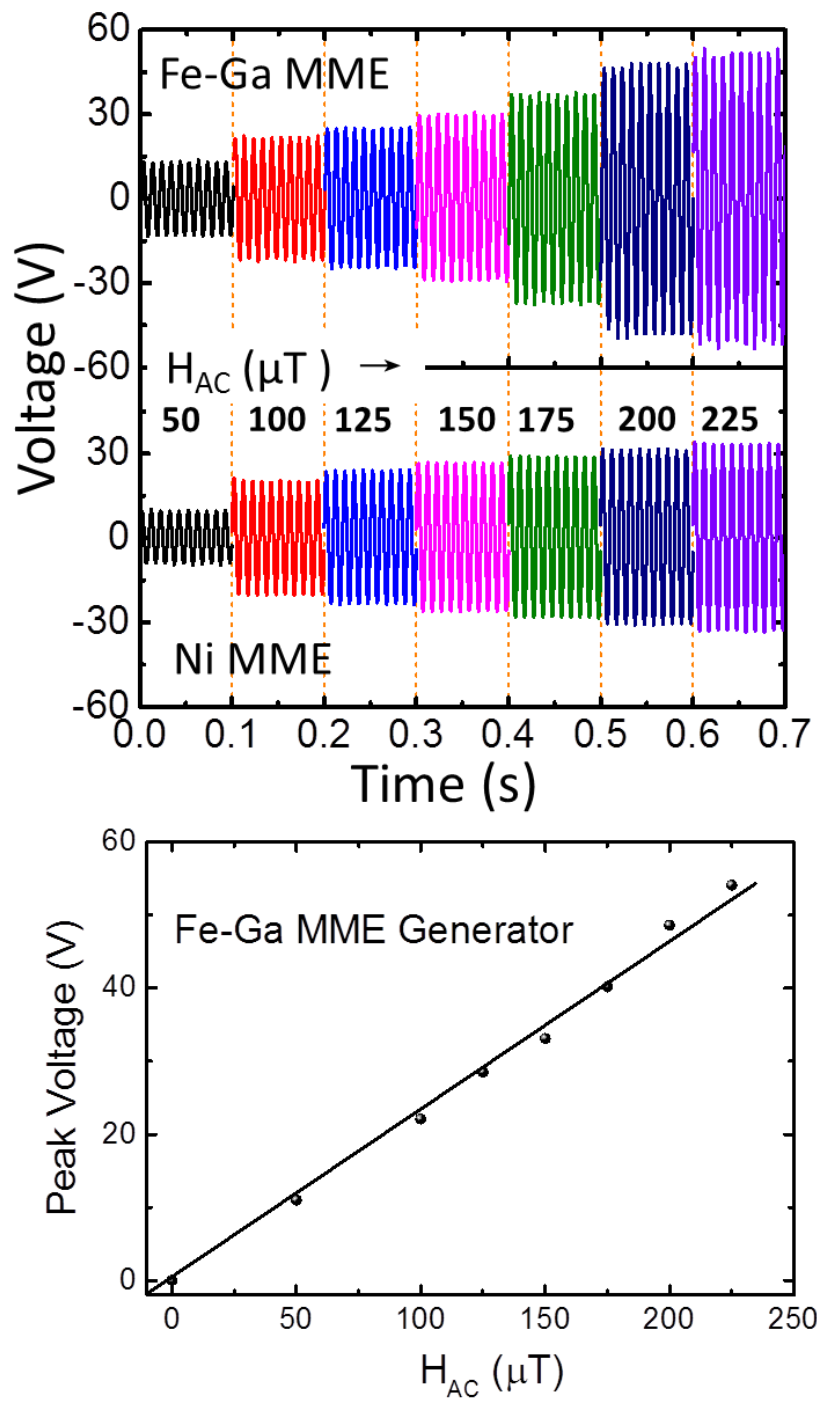


Figure S5. Open-circuit output voltage wave forms at different applied magnetic AC fields from 50 μT (0.5 Oe) to 225 μT (2.25 Oe) at an anti-resonance frequency of 100 Hz. The output performance of the MME generator linearly increased with the input magnetic AC field.

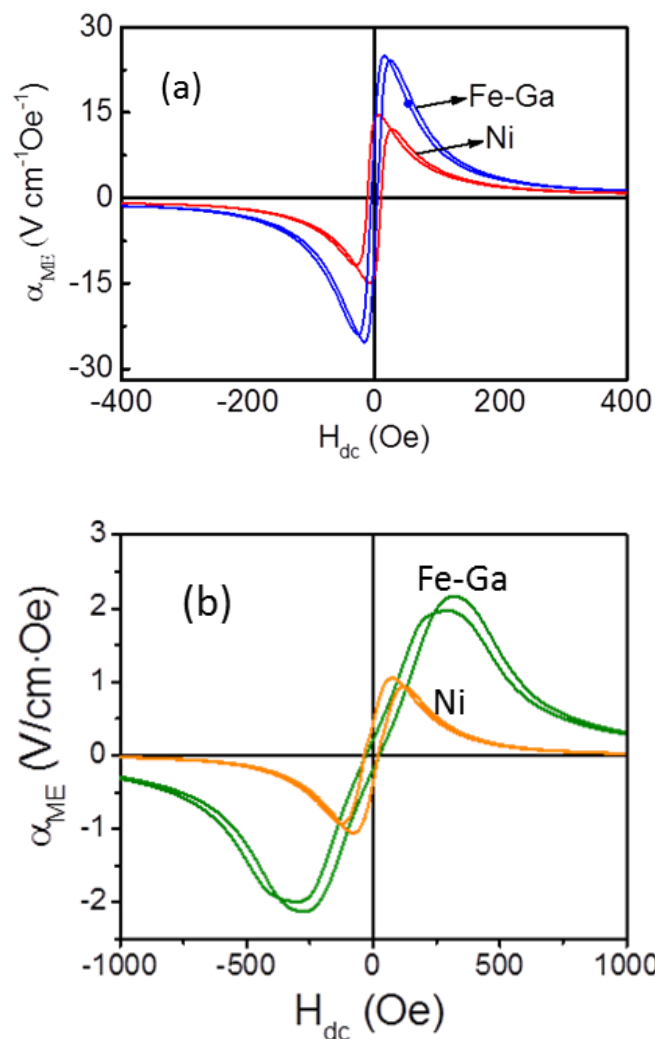


Figure S6. (a) ME responses of the bilayered cantilever structures in bending resonance mode (approximately 900 Hz). The maximum α_{ME} of the textured FeGa-based ME composite was approximately 26 $V \text{ cm}^{-1} \text{ Oe}^{-1}$, which was approximately 53% higher than that of the polycrystalline Ni-based ME composite. (b) ME responses of the trilayered composites of FeGa/PMN-PZT/FeGa and Ni/PMN-PZT/Ni with similar aspect ratios of magnetostrictive layers as that of bilayered composites.

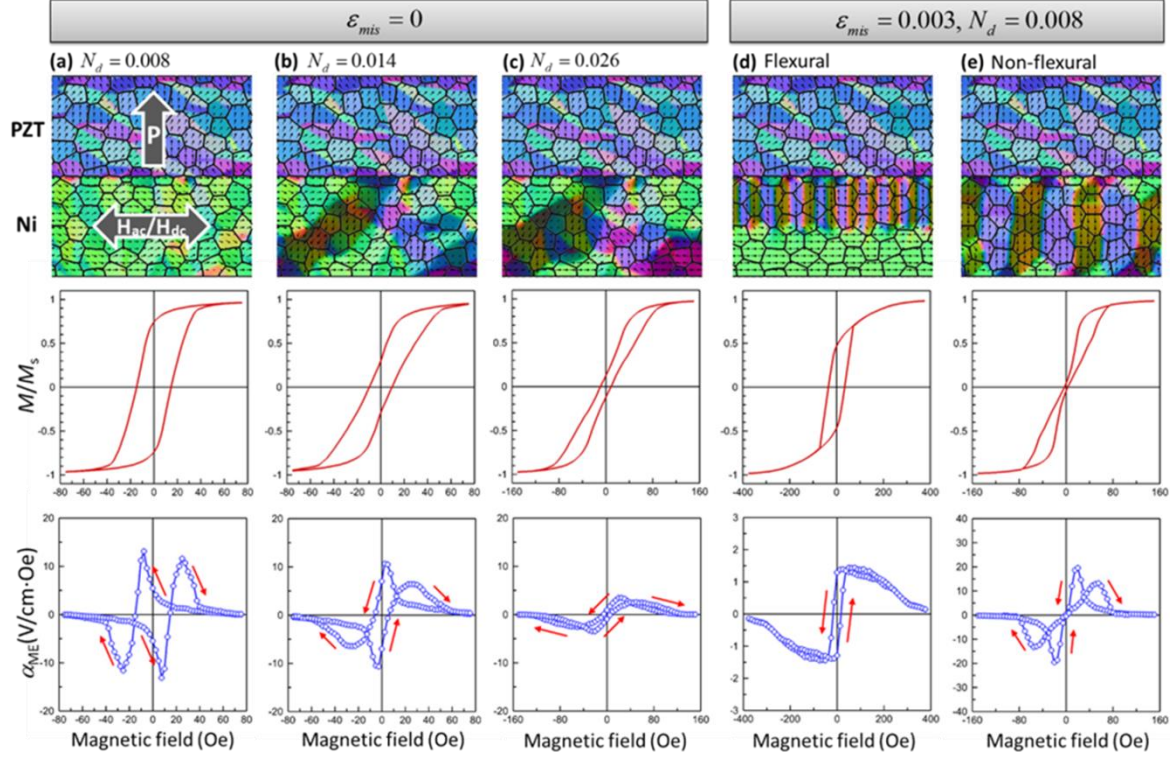


Figure S7. Phase-field model simulated domain structures (under zero magnetic bias), M-H hysteresis, and ME voltage coefficient α_{ME} for laminate PZT/Ni composite under zero mismatch strain $\varepsilon_{mis} = 0$ with varying demagnetization factors (N_d) in Ni layer of different thicknesses: (a) $N_d = 0.008$ ($t = 50 \mu\text{m}$), (b) $N_d = 0.014$ ($t = 100 \mu\text{m}$), and (c) $N_d = 0.026$ ($t = 200 \mu\text{m}$), and under mismatch strain $\varepsilon_{mis} = 0.003$ with the same demagnetization factor $N_d = 0.008$ in (d) flexural and (e) non-flexural composite. Domain patterns are visualized by color maps with red, green, blue (RGB) components proportional to P_x, P_y, P_z in PZT layer and M_x, M_y, M_z in Ni layer, respectively.[3]

Our phase-field modelling studies on PZT/Ni ME composites indicated that, the demagnetization in the magnetostrictive layer and flexural moment of the laminate structure greatly influence the magnetization behavior and ME response of the composites. In ME composites, it has been shown that $\alpha_{ME} \propto q_{ij} \propto \frac{dM^2}{dH}$ since $q_{ij} = \frac{d\lambda_{ij}}{dH}$ and $\lambda_{ij} \propto M^2$ through the relation $\varphi \sim \frac{3\sigma\lambda_{ij}}{K+2\pi M^2}$, where α_{ME} , q_{ij} , λ_{ij} , M , φ , σ , and K are the ME coefficient, piezomagnetic coefficient,

magnetostriction, magnetization , angle of magnetic moments, stress, and anisotropy constant, respectively.

For a finite non-spherical ferromagnet, the demagnetization factor is expressed as $N_d \approx (wt/l^2) (\ln(4l/(w+t))-1)$, where l , w , t are its length, width, and thickness, respectively. In the case of PZT/Ni composites, modification of the thickness (50, 100, 200 μm) of Ni layer was found to result in changes in the position and magnitude of α_{ME} of the composite (Figure S7(a)-(c)). By assuming a finite mismatch strain in the piezoelectric layer, a flexural composite corresponding to bilayer PZT/Ni that could bend under the mismatch strain while a non-flexural composite corresponding to trilayer Ni/PZT/Ni that could not bend (Figure S7(d)-(e)). These differences in deflection behavior of the bilayer and trilayer composites might have resulted in the differences in their ME responses.

In our experiments, trilayered ME composites of Ni/PMN-PZ-PT/Ni and Fe-Ga/PMN-PZ-PT/Fe-Ga were observed to exhibit a much lower self-biased ME response (Figure S6 (b)), compared to those obtained for bilayered ME composites of PMN-PZ-PT/Ni and PMN-PZ-PT/Fe-Ga, respectively (Figure S6 (a)). The above results suggest that the factors such as demagnetization, mismatch strain, and flexural moment should be optimized in order to achieve a high self-biased ME response in the composites.

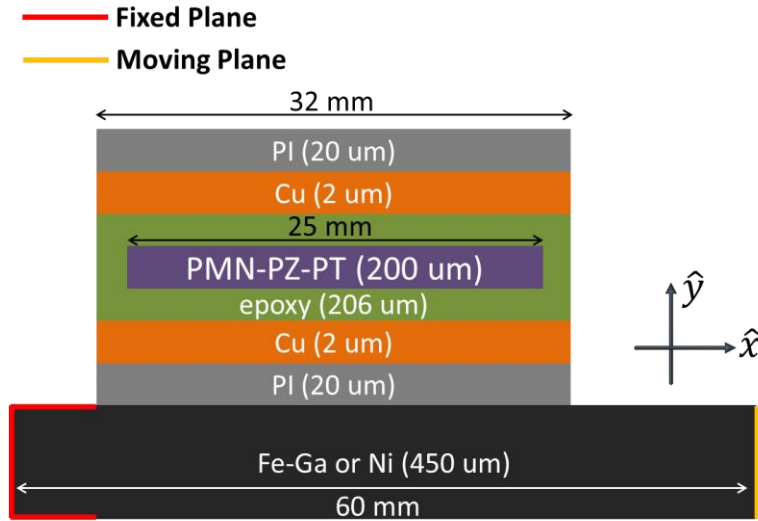


Figure S8. Model structure of the MME generators for COMSOL simulation.

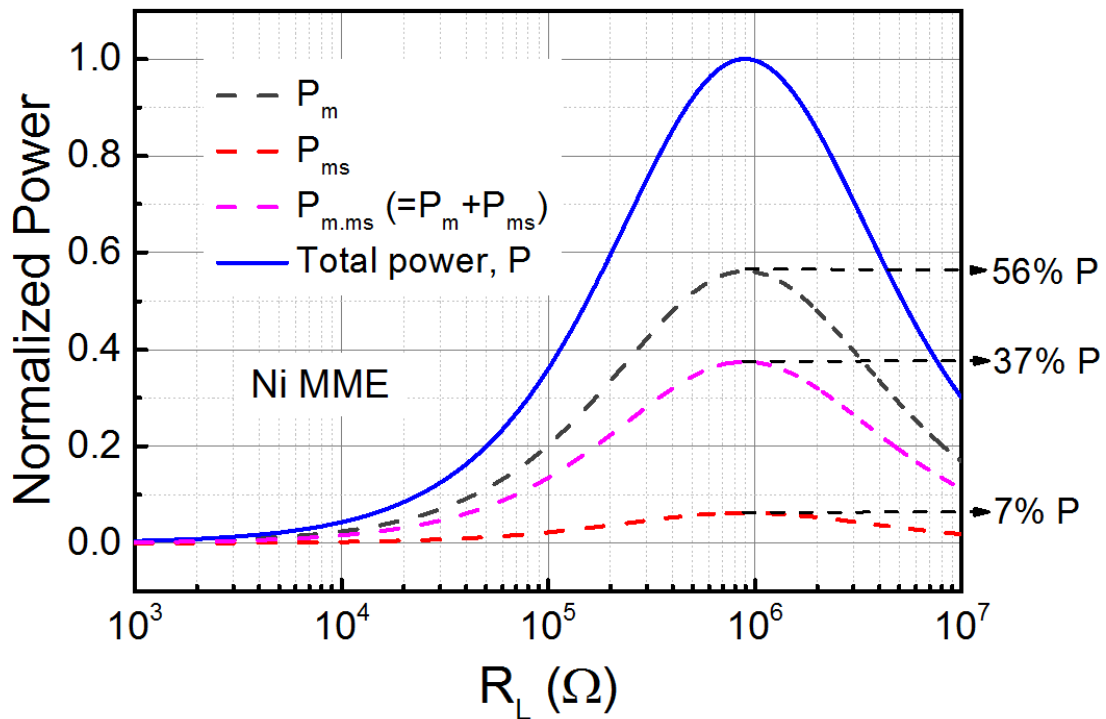


Figure S9. The power developed by Ni-based MME generator as a function of load resistance using Maxwell's equations.

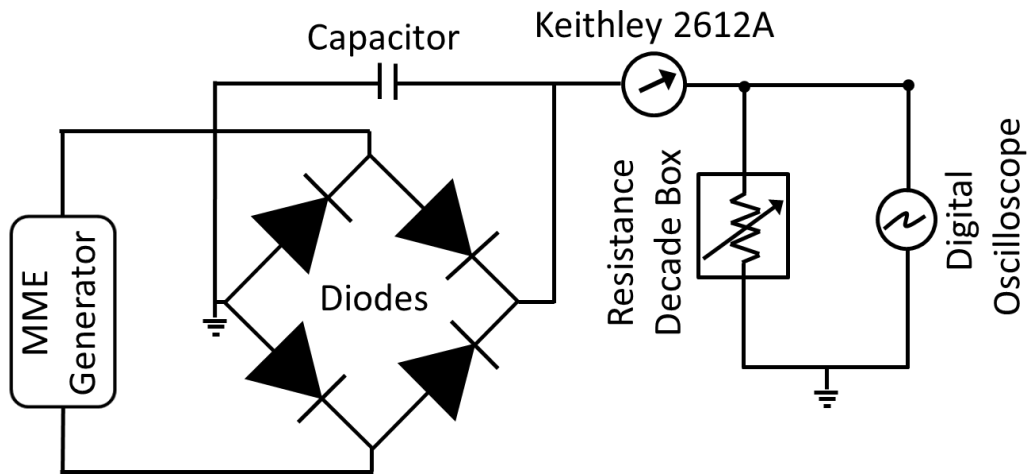


Figure S10. Schematic circuit diagram for measuring the output performance of the generator. The designed rectifying circuit system included the Fe-Ga MME generator, bridge rectifier, a capacitor, and external load. The output current and voltage were measured using a Keithley 2612A source meter and a digital oscilloscope, respectively.

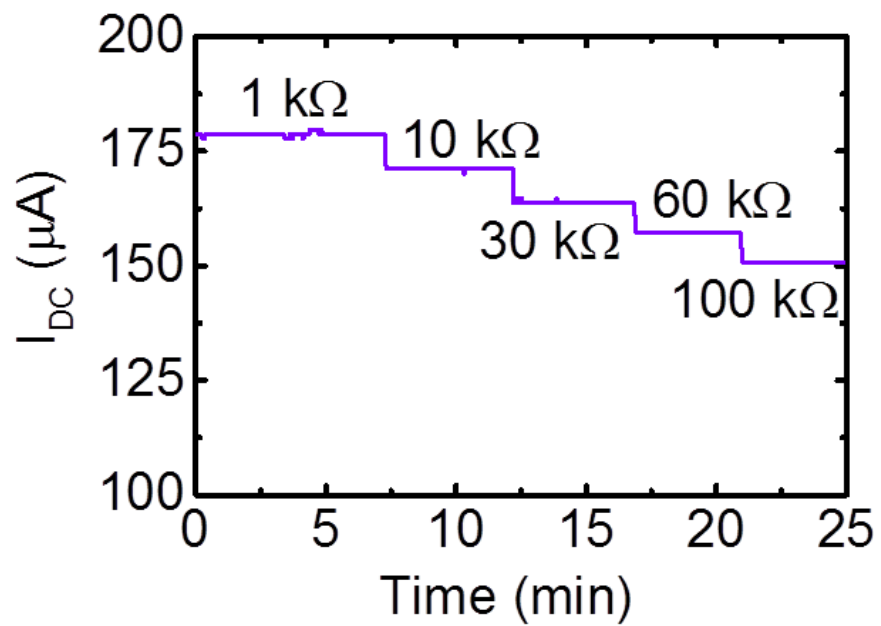


Figure S11. The output stability of the Fe-Ga-based MME generator under different output loads.

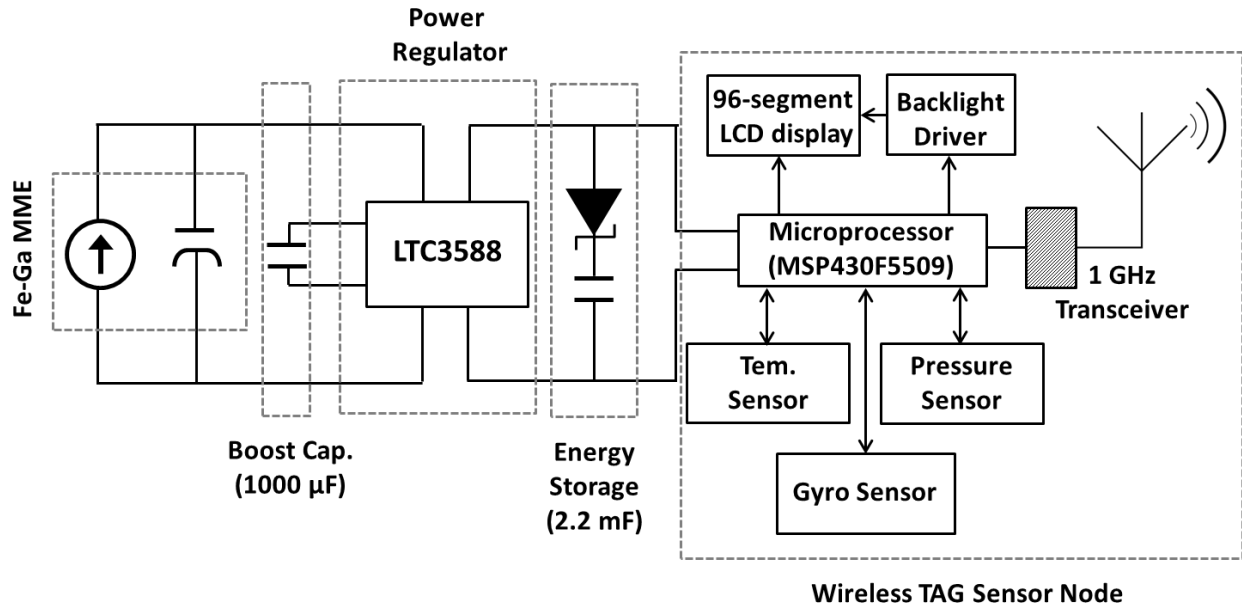


Figure S12. Schematic circuit diagram of the standalone-powered wireless IoT sensor system with triple-axis gyro (TAG), pressure, and temperature sensors, using the textured Fe-Ga MME generator.

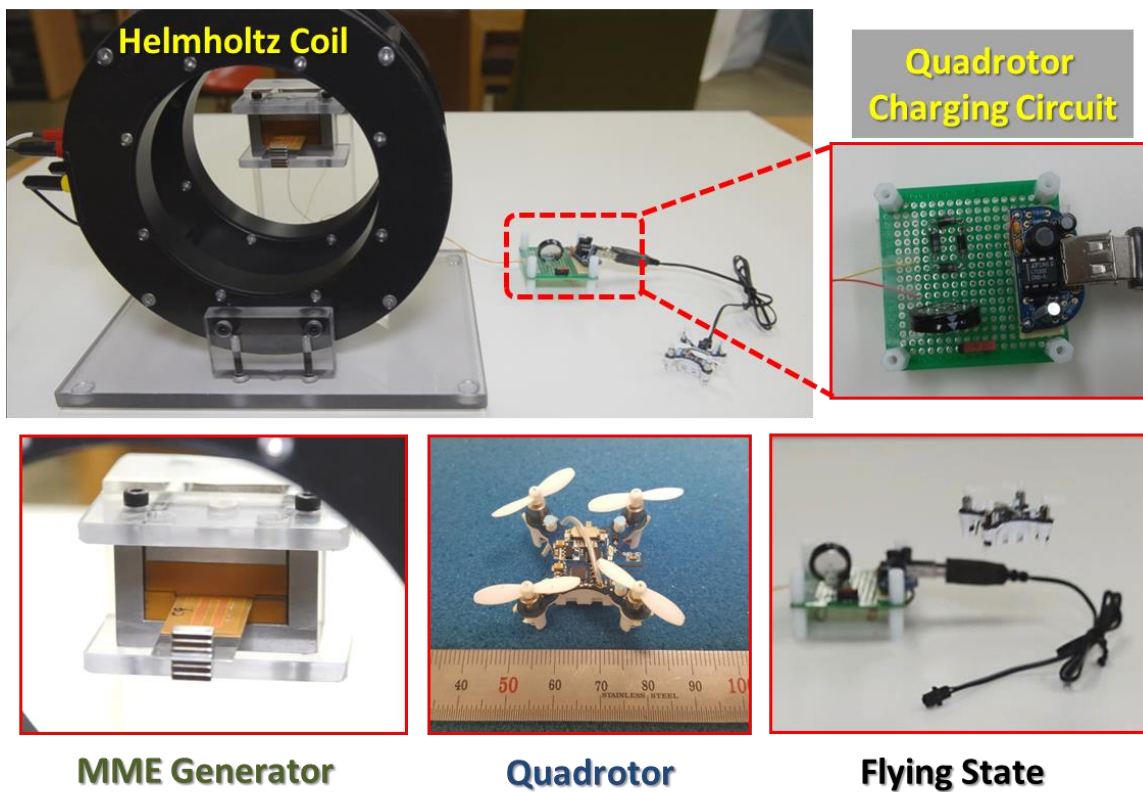


Figure S13. Snapshot images of the standalone-powered electronic circuit system and various parts of a small quadrotor drone operated with our Fe-Ga MME generator.

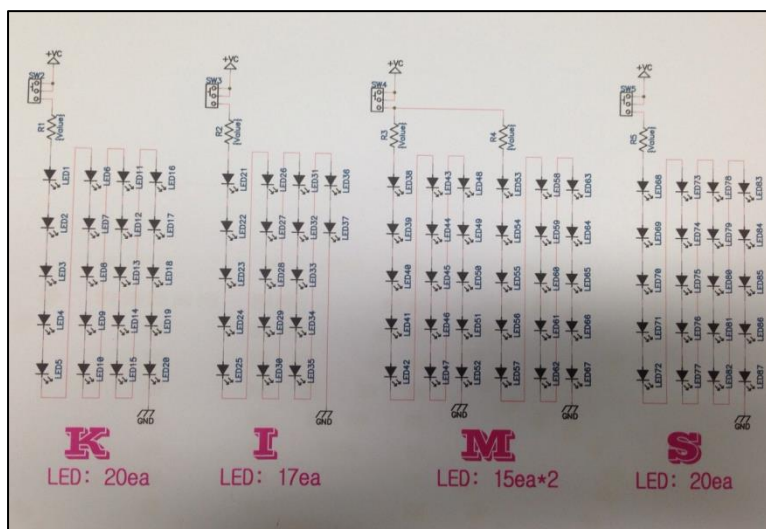


Figure S14. Schematic for LED sign board containing 174 high-intensity red LEDs.

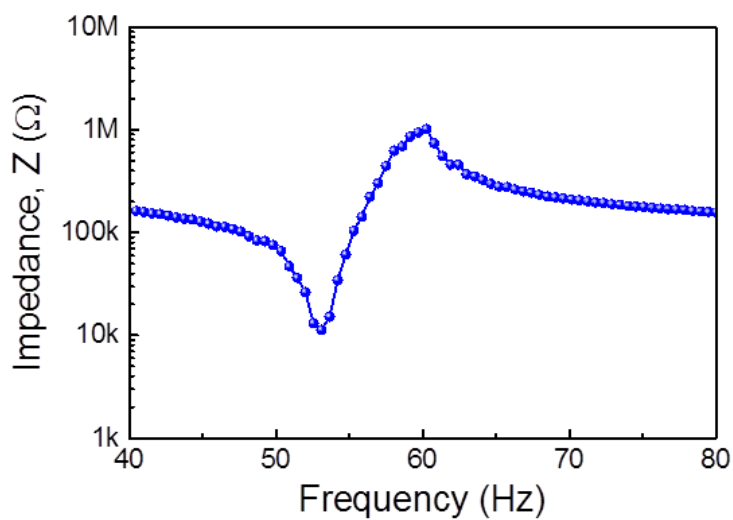


Figure S15. Impedance spectrum of the Fe-Ga MME generator

References

- [1] W. He, P. Li, Y. Wen, J. Zhang, A. Yang, C. Lu, J. Yang, J. Wen, J. Qiu, Y. Zhu, M. Yu, *Sensors Actuators A Phys.*, 2013, 193, 59.
- [2] P. Li, Y. Wen, P. Liu, X. Li, C. Jia, *Sensors Actuators, A Phys.*, 2010, 157, 100.
- [3] H. Palneedi, D. Maurya, L. D. Geng, H.-C. Song, G.-T. Hwang, M. Peddigari, V. Annapureddy, K. Song, Y.S. Oh, S.-C. Yang, Y. U. Wang, S. Priya, J. Ryu, *ACS Appl. Mater. Interfaces* (DOI: 10.1021/acsami.7b16706).